 doi:10.20944/preprints202011.0232.v2

Simulation of spatial strain inhomogeneities in lithium-ion-cells due to electrode dilation dependent on internal and external cell structures

Fabian Ebert*[1) 2)], Markus Spielbauer[2)], Maximilian Bruckmoser[2)], Markus Lienkamp[2)]

1) Fraunhofer Institute for Silicate Research ISC, Neunerplatz 2, 97082 Würzburg, Germany
(E-mail: ga32zij@mytum.de)

2) Institute of Automotive Technology, Technical University of Munich TUM, Boltzmannstraße 15, 85748 Garching, Germany

Abstract

Electrochemical-mechanical interactions, especially pressure-induced ones, have been identified to be a cause for lithium-plating in lithium-ion cells. Mechanically induced porosity inhomogeneities in the separator layers due to electrode expansion during charging especially lead to cell internal balancing currents and can cause localized plating. To identify cell-format and cell-material dependent mechanical weak spots, a layer-resolved mechanical simulation of different cell types and cell-material combinations is presented in this work. The simulation results show distinctive layer strain patterns for different cell-types that coincide with localized lithium-plating found in post-mortem cells. Additionally, the effects of cell bracing in battery modules is investigated and a method to mitigate the increased layer strain due to bracing counterforces is proposed that also increases cell energy density for hardcase-type automotive cells.

Keywords

Lithium-ion-cell; Electrode dilation; Mechanical strain; Cell-format; Layer resolved mechanical simulation

1. Introduction

Since the invention of the lithium-ion battery, battery cells have evolved in a multitude of form factors and electrode chemistries. For cylindrical cells, pouch-type cells and prismatic hardcase-type cells, the basic internal structure of commercially available cells remains the same. Most commercially available cell-types consist of a negative electrode (anode), a positive electrode (cathode) and an ion-conducting polymer separator soaked with electrolyte. Depending on the intended use, the composition of the electrodes and their layer thicknesses are varied. Cathodes nowadays are mostly either $LiCoO_2$ (LCO), $LiNi_xMn_yCo_zO_2$ (NMCxyz) or $LiNi_{0.8}Co_{0.15}Al_{0.05}O_2$ (NCA). Anodes consist predominantly of graphite and in some cases small amounts of added silicon to increase energy density [1]. Especially with added silicon, the dilation of the anode during operation is increased significantly. Where graphite shows a dilation between 4.3 % and 13.2 % (dependent on the measurement method) [2–7], silicon shows a dilation of around 300 % during lithiation [8,9]. Also, cathode materials show a dilation of -0.8 % to 0.9 % (NMC111) [2,10,11] or -2 % to -1.9 % (LCO) during lithiation [3,12]. On electrode material level, this dilation can e.g. lead to particle cracking which causes increased cell aging [13,14]. On cell level, electrode dilation can result in significant material strain; this can especially affect the soft polymer separator layers. Increased strain of the separator results in reduced porosity of the separator, which leads to increased internal resistance of the cell, but can also cause localized lithium-plating due to

Preprints (www.preprints.org) | NOT PEER-REVIEWED | Posted: 12 May 2021 doi:10.20944/preprints202011.0232.v2

mechanically induced balancing currents on electrode level [15–18]. Non-uniform/inhomogeneous pressure distribution was found to induce accelerated cell aging e.g. due to mechanically induced lithium plating [19–21]. In a worst-case scenario, electrode dilation can lead to creep and tearing of the separator with a subsequent thermal runaway by internal short circuits of the cell [22,23].

To investigate effects from macroscopic external and internal mechanical loads such as vibrations [24,25], shocks [24,26] and crush [27,28], a variety of simulative approaches have been conducted in the past, but only a few have investigated mechanical pressure on cell level [16,19,29,30]. Most publications use a homogenized model of the electrode stack, but only a few present electrode layer-resolved mechanical models as shown by the review of Kermani et al. [31]. When a layered model is used, often only a comparably small electrode stack section is modeled compared to the volume of the total electrode dimensions. Considering the mechanical variety of internal (round-wound, flat-wound or stacked electrode layers) and external (metal tube, foil-type or rigid prismatic-type) cell structures, homogenized models obviously have only limited explanatory power when investigating cell-format dependent effects like localized lithium plating. During post-mortem analysis of different cell types (Fig. 1), one can observe distinctive localized lithium-plating patterns for each cell type. Hence, the mechanical structure of a cell clearly has an impact on (spatial) lithium plating behavior.

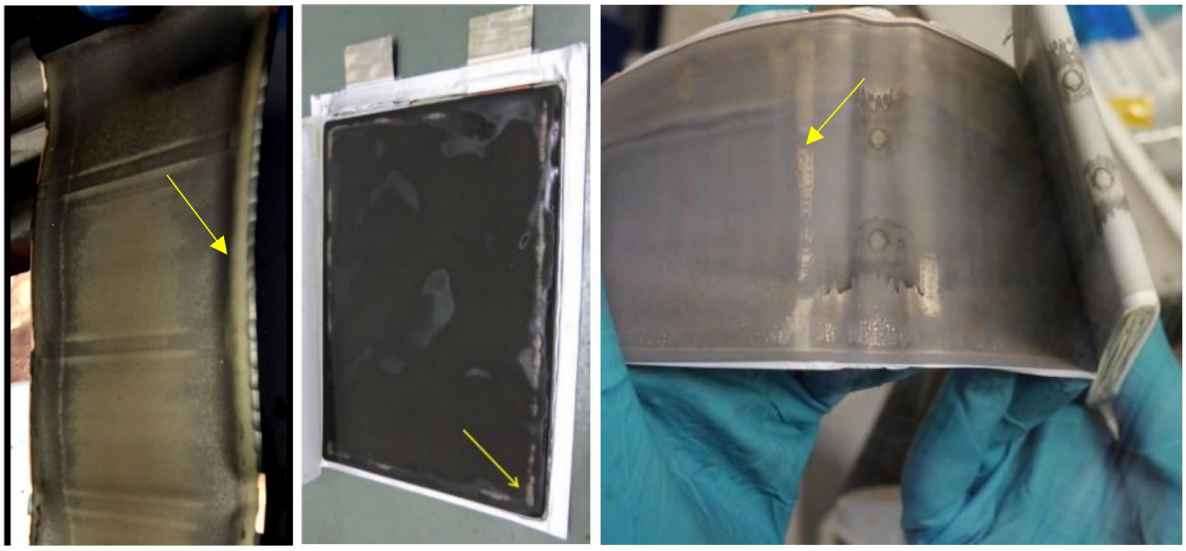

Fig. 1. (2 column) From left to right: localized lithium-plating patterns found in 18650-cell [15], pouch-type-cell [32] and prismatic hardcase-type cell [33].

In this work, an electrode layer resolved mechanical simulative study of common cell types and cell materials is presented that considers the variety of internal (electrode stack geometry) and external (casing or bracing structures in a battery module) cell structures. This boundary condition is also simulated with respect to ambient conditions in battery application, e.g. mechanically constrained cells in a battery module. Conclusively, an evolutionary approach to equate and reduce strain in battery cells is presented, which should decrease or even avoid mechanically induced balancing currents and therefore localized lithium-plating and increase cell lifetime.

 doi:10.20944/preprints202011.0232.v2

2. Material and methods

2.1. General modeling approach

All-in-all modeling of a lithium-ion-cell requires an electrochemical-mechanical coupled model which imposes high requirements regarding computational power, especially when dealing with an electrode-resolved model. To reduce the complexity of the model but get cell format dependent results, a pure finite-element mechanical simulation with Ansys 18.2 is conducted in this work. A summary of the used boundary definitions and simulation hypotheses can be found in the supplementary material (Table S.8 and S.9). Electrode dilation is simulated via parameterized virtual thermal material expansion. To investigate the maximum material strain at the end of the charging step, material dilation is simulated via a linear virtual temperature increase. Nonlinear dilation effects like graphite staging are omitted in this first study. Owing to the limitations of the used software version and for convergence of the model, some additional necessary simplifications are applied. Consequences of the simplifications for the results are discussed in detail in the discussion section.

The start of each simulation is a force-free state of an ideal cell with form-fit contact of the electrode/separator layers with the casing parts. Force generation due to binder swelling is neglected owing to only few available data. To investigate the mechanical stresses and strains of the electrode/separator layers in a charged cell, an isothermal single charging step of the cell is simulated. Therefore, thermal expansion of the material e.g. due to high charging currents is neglected. Since locally increased ionic resistance leads to localized balancing currents and therefore can cause localized lithium plating, the increased ionic resistance of the strained layers is calculated from the data of Sauerteig et al. [34].

2.2. Material models

Since electrodes consist of a porous matrix of largely active material and binder, mechanical material data from only the active material particles cannot be used. This is aggravated by the fact that, compression tests of electrodes show substantial differences in terms of mechanical stiffness compared with Young's modulus of pure active materials [34,35]. Therefore, lithiation hardening of active materials is neglected in this work as well. For this work, experimentally obtained stiffness data [34] obtained from electrode and separator compression tests is used and extrapolated to a maximum stress of 40 MPa. Material strain is calculated via integration of the material stiffness curves. For electrode dilation during lithiation values of 7.5 % (graphite anode without silicon) [2], 0 % (NMC111 cathode) [10] and -1.9 % (LCO cathode) [3] that were obtained from dilatometric experiments are used.

Experiments showed expansion only of the electrode perpendicular to the electrode thickness, hence dilation of the material is simulated orthotropic [36]. The binder material (usually polyvinylidene fluoride PVdF) of the electrodes and the separator materials (usually polyethylene PE or polypropylene PP) show visco-elastic behavior when stressed [37,38]. Owing to the only few available datasets and for the sake of simplicity of the model, material strain is simulated linear elastic in this work. The consequences for the results of this simplification is discussed in detail in the discussion section. The material parameters used for the polymeric materials can be found in the supplementary material (Table S.7).

Preprints (www.preprints.org) | NOT PEER-REVIEWED | Posted: 12 May 2021 doi:10.20944/preprints202011.0232.v2

2.3. Cell models

To investigate commonly available cell types, four different mechanical models are simulated (Fig. 2). Mechanical dimensions of the cell models can be found in the supplementary material for better readability of the article (Table S.1 – Table S.6).

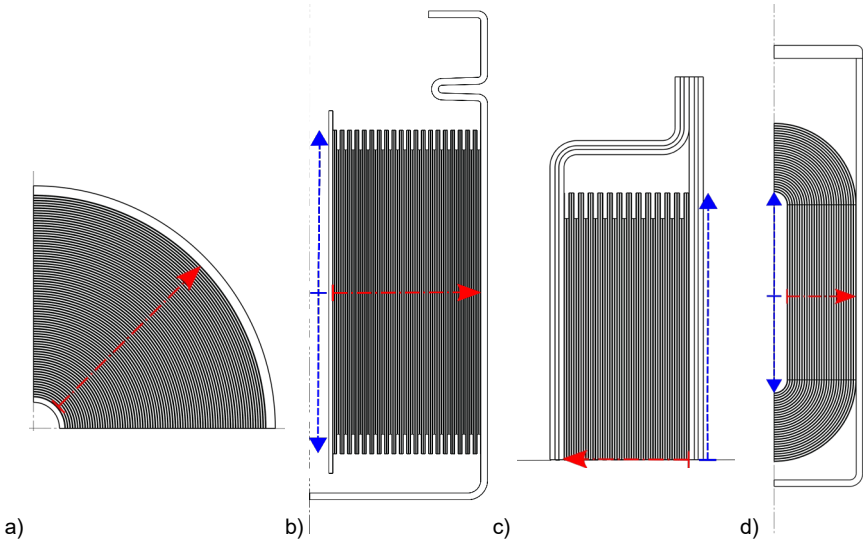

Fig. 2 (2 column) Illustration (not true to scale) of an 18650-cell cross section model a), longitudinal cross-section models of an 18650-cell b), pouch-type cell c) and hardcase-type cell d) with symmetry borders (black dashed lines). The red dot-dashed arrows mark the layer counting direction. The blue dashed arrows mark the position on the layer used in the longitudinal cross-section modeling with the center position marked.

First, a quarter cross-sectional model of an 18650-cell is simulated (Fig. 2a), which allows a reduction of nodes owing to its radial symmetry. The outer casing of the cell and the winding mandrel in the center are composed of stainless steel. The electrode stack consists of repetitive layers of copper current collectors, anode layers, separators, cathode layers, aluminum current collectors, cathode layers, separators and anode layers. The outmost layer is modeled as a copper current collector layer as often found in commercial cells. Since especially cylindrical cells come in a variety of cell material variants, not only the mechanical effects from different cathode materials (LCO vs. NMC) but also the behavior of different separator materials (PP vs. PE separator) is simulated. Additionally, the effect of two different common electrode configurations (high Energy (hE) configuration with high electrode loading and high Power (hP) configuration with less electrode loading for better performance at high currents) is investigated. Finally, the effect of the cell diameter (18650 vs. 21700 cell) is surveyed.

To simulate effects near the edge of the cell casing or e.g. due to anode overlap, longitudinal section models of either an 18650 cell (Fig. 2b), a pouch-type cell (Fig. 2c) and a hardcase-type cell (Fig. 2d) are conducted. Just like with the cross-section model, a rotational symmetry axis is used to reduce the number of nodes and hence computing time and memory usage.

The outer shell of the simulated pouch-type cell consists of a three-layer laminate of PE/Aluminum/PE in this work. To simulate the stiffening of the cell during vacuum sealing in production, a preload of 95 kPa is applied to the outer shell before the virtual charging of the cell.

The casing of the simulated hardcase-type cell consists of aluminum. The dimensions of the cell are like those in the cells used in mild-hybrid vehicles (HEV). Owing to the flat-wound structure of the electrode stack, a hollow part forms in the center of the cell. Since this can lead to layer detachment during the modeled charging step, which is adverse for model convergence, the area is filled virtually

Preprints (www.preprints.org) | NOT PEER-REVIEWED | Posted: 12 May 2021 doi:10.20944/preprints202011.0232.v2

with a soft HT800 (Rogers Bisco) silicon foam material. Owing to the comparably low stiffness of the foam material compared with other cell materials, results should only be distorted marginally.

Due to the large number of nodes of the layer resolved model, the mesh size must be carefully chosen to limit computing time and memory usage. A preliminary convergence study of the cross-section of an 18650-model showed satisfying convergence results when one element per layer (relating to layer thickness) is used (Figure S.4). For the longitudinal model, a sectioned mesh with finer mesh size must be used to get a good convergence in areas of high stress/strain, e.g. near the cathode layer edge and the separator. A convergence study showed suitable convergence for ten elements per layer (relating to layer thickness) (Figure S.5). For the remaining model areas five elements per layer are used to reduce computing time and memory usage.

2.4. Modeling effects in a battery module and mechanical cell improvement

In laboratory aging test setups, single cells are often tested without mechanical constraints. Owing to additional mechanical loads e.g. vibration in applications like an electric car, pouch-type and prismatic hardcase-type cells are bundled to cell modules and braced by a rigid module construction. This stiff module construction obstructs the outward dilation of the cells during charging and aging. As a result, the internal stresses and strains increase owing to the counterforce of module bracing [19,39] compared with an unbraced cell. To investigate this scenario, virtual ideal module bracing is applied to the simulated cell by predefining the outer casing as fixed.

Additionally, as an approach to moderate the assumingly increasing stresses and strains because of the module construction, braced cells with a HT-800 silicon foam layer are simulated instead of some outermost cathode/separator/anode layers to allow a certain amount of electrode dilation. In case of the prismatic hardcase-type cell, the void in the center is filled with the foam as well. The separator and the foam materials are simulated via an Ogden-foam model (parameters in supplementary material Table S.7). Tab. 1 shows an overview of the simulations conducted for this work.

Tab. 1 (2 column) Overview of simulated cell types.

	Variant 1	Variant 2	Variant 3	Variant 4
Cross-sectional simulations (cylindrical cell)	high Energy (hE) vs. high Power (hP) electrode configuration	PE vs. PP Separator (high Energy (hE) configuration)	NMC vs. LCO cathode (high Energy (hE) configuration)	18650 vs. 21700 format (high Energy (hE) configuration)
Longitudinal-cross-sectional simulations (all high Energy (hE) configuration)	18650-type cell			
	Pouch-type cell (unconstrained)	Pouch-type cell (constrained)	Pouch-type cell (constrained with elastomer layer)	
	Hardcase-type HEV cell (unconstrained)	Hardcase-type HEV cell (constrained)	Hardcase-type HEV cell (constrained with elastomer layer)	
	Stacked hardcase-type HEV cell (unconstrained)	Stacked hardcase-type HEV cell (constrained)	Stacked hardcase-type HEV cell (constrained with elastomer layer)	

Preprints (www.preprints.org) | NOT PEER-REVIEWED | Posted: 12 May 2021 doi:10.20944/preprints202011.0232.v2

3. Results and Discussion

3.1. Effects of electrode material variation and cell sizing of cylindrical cells

A cylindrical cross-section model allows for the investigation of the variation of material characteristics with tolerable computational effort owing to the comparably small number of simulation nodes.

First, the differences of the behavior of a cell with a high-energy (hE) configuration (high electrode loading for high energy density) and a cell with high-power (hP) configuration (thin electrode loading for low internal resistance) are investigated (Fig. 3a-c). Layer number zero denotes the innermost layer of the cell next to the mandrel. Owing to the similar outer diameter of the cell, but the thinner electrode loading, the high-power cell contains a higher number of layers. The final strains after charging of the cell in the separator layers for high-energy configuration (Fig. 3a) show an average layer compression of 8.5 % with an increase of ionic resistance of 26 % for the inner layers and 20 % for the outer separator layers. The separator layers of the high-power cell show an average compression of 7.5 % with an increase of ionic resistance of 19 % for the inner layers and 15 % for the outer separator layers. For the anode layers (Fig. 3b), the virtual charging of the cell results in an average compression of 3 % with an average ionic resistance increase of 26 % (hE) and an average compression of 2.8 %, with an average ionic resistance increase of 21 % (hP). For the cathode layers, (Fig. 3c) the virtual charging of the cell results in an average compression of 3.5 % with an average ionic resistance increase of 10 % (hE) and an average compression of 3 % with an average ionic resistance increase of 9 % (hP).

When exchanging the PE-separator used before with a stiffer PP-separator (both hE-configuration), the average compression of the separator layers (Fig. 3d) decreases to 1.5 % and the compression spread also decreases. The increase of ionic resistance for the PP-separator is not calculated, because no ionic resistance data is available for this separator material. Owing to the stiffer PP-separator, the average compression of the anode layers increases to 3.8 % with an average ionic resistance increase of 48 % (Fig. 3e) and for the cathode layers (Fig. 3f), the simulated charging of the cell results in an average compression of 4.8 % with an average ionic resistance increase of 16 %.

When exchanging the NMC-cathode used before with an LCO-cathode (both hE-configuration) the average compression of the separator layers (Fig. 3g) increases to 11 % owing to the additionally expanding cathode during the simulated charging of the cell. The average increase of ionic resistance for the separator layers increases to 38 %. The average compression of the anode layers increases to 3.4 % with an average ionic resistance increase of 25 % (Fig. 3h), and for the cathode layers, the virtual charging of the cell results in an average compression of 4 % (Fig. 3i). Owing to non-available data, the ionic resistance increase for the LCO cathode was not calculated.

Preprints (www.preprints.org) | NOT PEER-REVIEWED | Posted: 12 May 2021 doi:10.20944/preprints202011.0232.v2

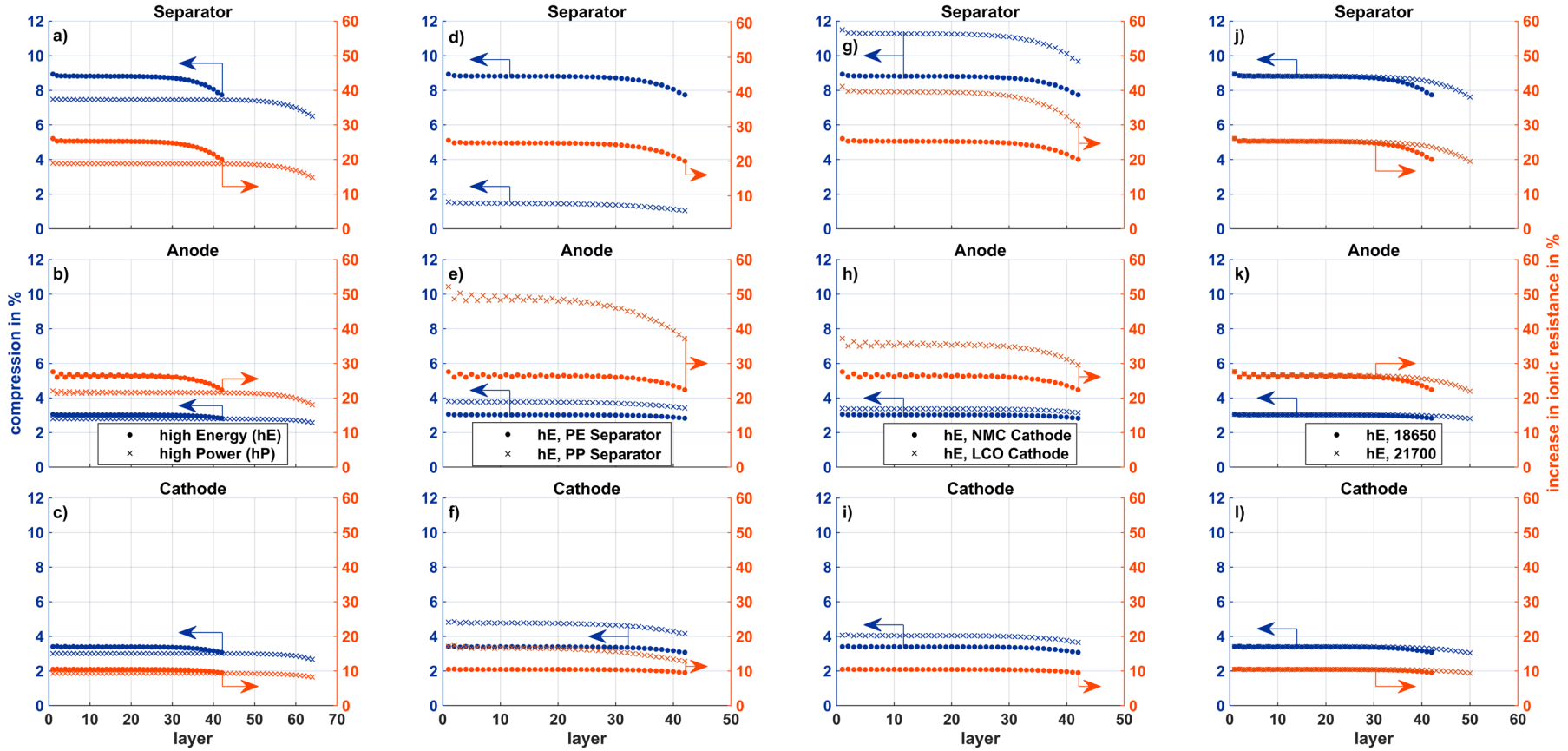

Fig. 3 (2 column) Calculated layer strains and ionic resistance increases after simulated charging step with the cross-sectional model of an 18650-cell. Each column represents a whole cell (anode/separator/cathode part): a-c) Comparison of a high Energy (hE) vs. high Power (hP) configuration; d-f) effects of two different separator materials (PP vs. PE in high Energy electrode configuration); g-i) effects of two different cathode materials (NMC vs. LCO in high Energy electrode configuration); j-l) comparison of an 18650 and an 21700 cell (in high Energy (hE) electrode configuration).

Preprints (www.preprints.org) | NOT PEER-REVIEWED | Posted: 12 May 2021 doi:10.20944/preprints202011.0232.v2

When comparing an 18650 cell with an 21700 cell (both hE-configuration), similar results in terms of layer compression and increase of ionic resistance emerge (Fig. 3j-l) despite the higher number of layers in the 21700 cell (50 vs. 42) and the increased cell diameter. Compared with the 18650 cell, one can observe a widening of the constant compression plateau in the middle of the jellyroll and the pressure distribution in the outer layers. For an overview of the results see Tab. 2.

Tab. 2 (2 column) Simulation results overview of electrode material variation and cell size of cylindrical cells.

Average layer compression in %	Separator	Anode	Cathode	**Average increased ionic resistance in %**	Separator	Anode	Cathode
high Energy cell (hE) 18650 size w/ PE separator, NMC cathode	8.5 %	3.0 %	3.5 %	**high Energy cell (hE)** 18650 size w/ PE separator, NMC cathode	+25 %	+26 %	+ 10 %
high Power cell (hP) 18650 size w/ PE separator, NMC cathode	7.5 %	2.8 %	3.0 %	**high Power cell (hP)** 18650 size w/ PE separator, NMC cathode	+18 %	+21 %	+ 9 %
high Energy cell (hE) 18650 size w/ PP separator, NMC cathode	1.5 %	3.8 %	4.8 %	**high Energy cell (hE)** 18650 size w/ PP separator, NMC cathode	no data available	+48 %	+16 %
high Energy cell (hE) 18650 size w/ PE separator, LCO cathode	11 %	3.4 %	4.0 %	**high Energy cell (hE)** 18650 size w/ PE separator, LCO cathode	+38 %	+25 %	no data available
high Energy cell (hE) 21700 size w/ PE separator, NMC cathode	8.5 %	3.0 %	3.5 %	**high Energy cell (hE)** 21700 size w/ PE separator, NMC cathode	+25 %	+26 %	+ 10 %

In terms of layer compression amplitude and incline of ionic resistivity, the high-power cell shows advantages for the anode, cathode and the separator (for the simulated configuration). This is driven mainly by the fact, that the percentage of active material is lower compared with the high-energy cell, hence less dilation of the electrodes in total. To increase the energy density in high-power cells and decrease the ionic resistivity of the cell from a mechanical position, the use of thinner separators is possible. The usage of a stiffer separator material like PP is favorable in terms of separator compression behavior, but not in terms of cost of the compression and therefore the increase of ionic resistance of the anode and cathode layers. The soft anode layer especially sees almost double the increase in ionic resistance in this scenario. For cell manufacturing or when solid electrolytes are used in the future, this must be considered e.g. by manufacturing electrodes with a higher porosity to maintain the same ionic resistivity compared to a softer separator material. When a cathode material like LCO is used that adds further expansion during cell charging, extra strain is added during charging and therefore the ionic resistance of all active layers of the cell increases significantly. A similar scenario is the usage of anode materials with higher expansion like silicon blended graphite anodes. The results of the simulation of 18650 and 21700 cells with the identical electrode formulation are comparable in terms of maximum layer strain and inhomogeneity.

The simulation results only show the effect of a single charge of a virtual cell. Effects from cell aging, especially irreversible anode dilation [2], are not examined in this investigation. To investigate

 doi:10.20944/preprints202011.0232.v2

transient effects, nonelastic behavior of the binder and separator material should be simulated in the future as a next step. Nevertheless, macroscopic effects on cell level can be estimated from transient material behavior itself without numerical simulation. Owing to the visco-elastic nature of the binder and separator materials [37,38], the maximum amount of stress will decrease progressively at the expense of layer strain. Since anode hardening due to increased SEI formation over time [34], the soft separator will be the most strained material in the cell. The simulation results presented here thus show an attenuated scenario in terms of layer strain and ionic resistance increase. Layer strain and ionic resistance, especially of the separator layers, will be significantly increased in aged cells.

For evaluation of different material pairings (anode/separator/cathode), the usage of a simplified cross-section model allows for a comparable fast screening for mechanically driven effects on material level. Since the electrode and separator layers are simulated not as a spiral but as closed rings in the quarter cell model, the stiff current collector layers shield expansion of the inner active material layers to some extent. In a real cell, the strain of the inner layers should be lower than depicted in the results. especially when there is no mandrel present in the cell and relative electrode movement is possible [40].

Since the cross-sectional model cannot reproduce effects like e.g. stiff casing corners, for the following investigations of longitudinal cross-section models (high-energy electrode configuration with a NMC-cathode and a PE-separator) are used. When looking at the results of the longitudinal cross-section model of the 18650 cell (Fig. 4a), one can observe an increase of layer compression, especially near the casing edges of the cell, with peaks of over 9 % compression before the compression drops to zero for the separator parts without contact to electrodes (overlap regions). The peaks are caused by the overhang of the anode over the cathode layers at the position of the edge of the cathode layer where the separator layer is compressed owing to electrode dilation.

To verify the usability of the longitudinal cross-section model, the values of the layer compression of both approaches (Fig. 4d) are compared for the midsection of the cell (x-position zero denotes the location of the horizontal symmetry axis of the jellyroll at 50 % cell height). The calculated values for layer compression of both models show good comparability with a maximum deviation of less than 0.5 %.

Preprints (www.preprints.org) | NOT PEER-REVIEWED | Posted: 12 May 2021 doi:10.20944/preprints202011.0232.v2

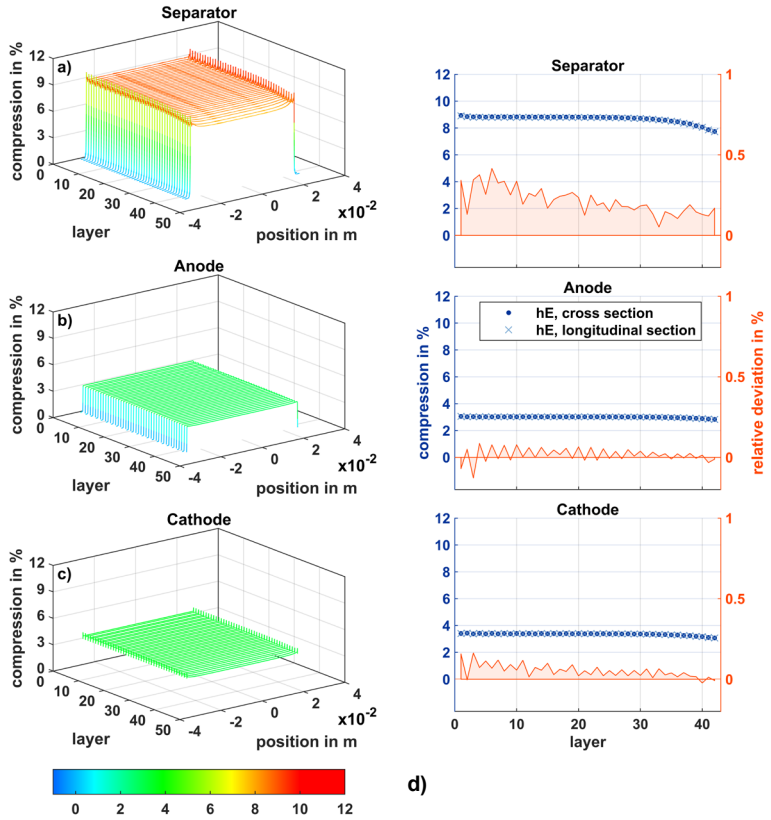

Fig. 4 (2 column): a-c) Strain in a longitudinal cross-section model of an 18650 cell. d) Deviation calculation between the radial cross-section simulation and the longitudinal cross-section simulation at position zero (50 % cell height).

When investigating cells on a more macroscopic level, the usage of longitudinal cross-section models is imperative because of border effects like rigid casing edges that cause inhomogeneous counter stress during electrode dilation. The results of the longitudinal simulation show high gradients in separator strain in the anode overlap region. From a purely mechanical point of view, this is disadvantageous, but it is necessary from an electrochemical point of view to avoid deficient covering of the anode and the hereby caused lithium plating [41].

3.2. Effects due to module bracing for different cell formats

Since the increase of ionic resistance scales almost linearly with material strain, only the layer strain is shown for better clarity of the figures in the following.

When looking at the results of a virtual charge step of an unconstrained pouch cell (Fig. 5a), one can observe a low layer compression of only 1 % for most areas of the cell. Peaks in layer compression can only be observed near the edge of the cell, and especially in the outer electrode stack area. Additionally, next to the peaks in inward direction of the cell, an area of reduced layer compression can be found mainly in the outer layers. In a constrained cell (Fig. 5b), compression of the separator layers rises to around 9 % and 3 % for the anode and cathode layers, respectively. Compared with the unconstrained cell, the compression of the layers is more homogeneous. As with the 18650 cell, distinctive peaks due to the anode overlap can be found in the pouch-type cell as well. The partly

Preprints (www.preprints.org) | NOT PEER-REVIEWED | Posted: 12 May 2021 doi:10.20944/preprints202011.0232.v2

higher compression values of the inner cathode layers are simulation artifacts due to contact chattering.

When only a few electrode layers of the braced cell are exchanged with a silicon foam layer with a thickness of 470 µm (corresponds to twice the cell dilation at free expansion) and the length of the cathode layers is added (see supplementary material Figure S.1) to allow electrode dilation, a uniform and low compression (< 1 %) scenario can be observed even though the cell is constrained (Fig. 5c). Owing to the comparably low stiffness of the foam material, the compression of the electrode and separator layers is nearly zero, but low compression is maintained in the charged cell.

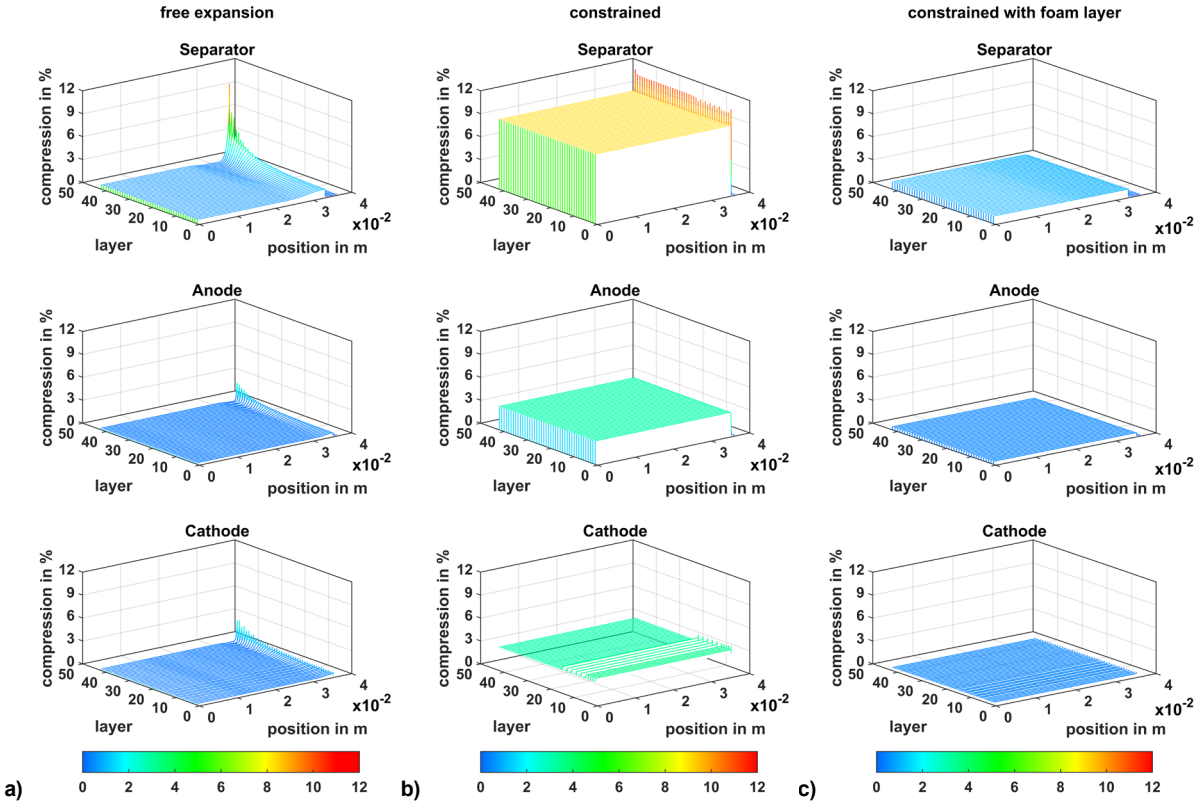

Fig. 5 (2 column): a) Final layer strain of an unconstrained pouch-type cell, b) a constrained pouch-type cell and c) a constrained pouch-type cell with a foam layer to allow electrode expansion despite the constrained cell.

When comparing the strain maps of the three different scenarios, differences between unconstrained cells and constrained cells found in aging investigations [19,20] are understandable. Although the low compression in most areas of the cell seems promising at first glance, the high compression gradients near the edge of the cell lead to cell-internal balancing currents due to locally reduced electrode and separator porosity [15,42]. Additionally, at the area of lower compression in the outer edge of the cell, delamination of the electrode and separator layers can occur, which would be visible in the mechanical model as negative compression. Since (local) layer delamination completely disrupts ionic conductivity, lithium plating occurs predominantly in these areas. Therefore, delamination must be avoided e.g. via constructive measures like appropriate module bracing. Under the delamination and compression gradient avoidance aspect, a homogeneous stress/strain simulation result in a constrained cell should be targeted. As shown in previous investigations [19,20], cell aging accelerates with increased external pressure, which is equal to cell-internal pressure in the case of the pouch-type cell owing to a missing rigid barrier as for cylindrical and hardcase-type cells. A low layer compression of a few ten kilopascals

Preprints (www.preprints.org) | NOT PEER-REVIEWED | Posted: 12 May 2021 doi:10.20944/preprints202011.0232.v2

should therefore be targeted [20]. To comply with the need to fasten cells in applications like electric cars, the presented enhanced cell with a compressible layer such as foam could be a promising alternative. Depending on the foam layer thickness, even irreversible dilation due to cell aging can be compensated. As investigations have shown, flexible bracing with a constant bracing force slows cell aging significantly compared with rigidly braced cells [19]. For applications, the widely inert (except for the presence of significant amounts of hydrofluoric acid) silicon foam can be applied cell-internal but also cell-external owing to the flexible pouch-type foil casing. Not only is the thickness of the foam layer important, but also the lateral dimensions. When the foam layer is sized equal to the anode layers, a compression scenario comparable with the free expanding cell can be observed as the foam overlaps the cathode edges (see supplementary material Fig. S.2).

As with the pouch-type cell, three scenarios are again simulated for the hardcase-type cell (Fig. 6).

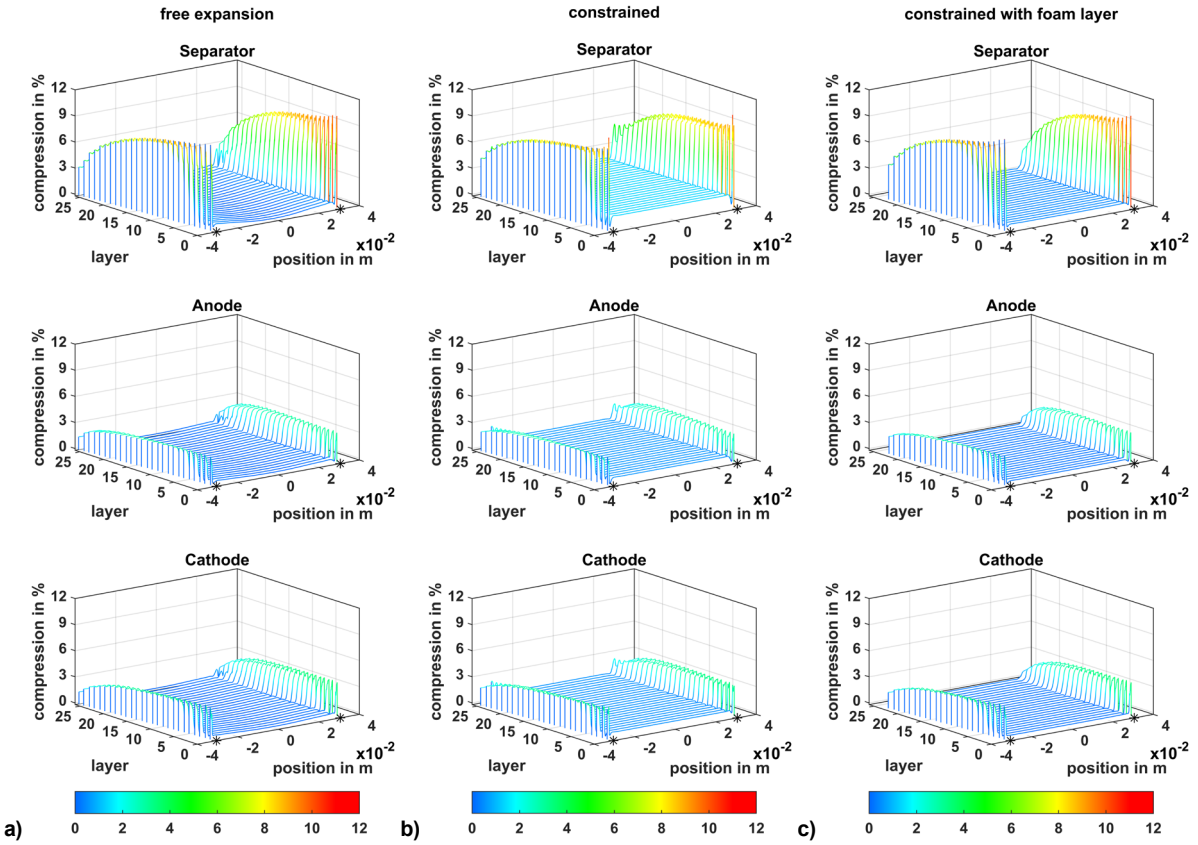

Fig. 6 (2 column): a) Final layer strain of an unconstrained hardcase-type HEV cell, b) a constrained hardcase-type HEV cell and c) a constrained hardcase-type HEV cell with a foam layer to allow electrode expansion. The asterisks mark the outermost contacts of the jellyroll with the cell casing before the bent sections begins.

For the unconstrained cell (Fig. 6a), one can observe low compression of around 1 % for the electrode and separator layers independent of the layer numbers regarding the center area. Compression peaks can be found in the curved areas of the jellyroll with a maximum 10 % compression of the separator layers in the center layers of the jellyroll, where small winding radii occur. Compression of the electrode layers is as high as 3 % in this area. For the outer layers, the compression peaks of the curved electrode and separator parts decrease, because the layers can expand freely (non-existing contact with the cell casing in this area). As with the unconstrained pouch-type cell, a section of comparable low compression can be found next to the compression peaks. The likelihood of layer delamination or plating due to mechanically induced balancing currents is expected to be significantly higher here. For

Preprints (www.preprints.org) | NOT PEER-REVIEWED | Posted: 12 May 2021 doi:10.20944/preprints202011.0232.v2

the curved electrode and separator areas, the compression behavior is comparable with cylindrical cells.

When the cell is constrained (Fig. 6b) on the long side, only a small increase in layer compression can be observed. Only the flat mid-section with contact to the cell casing is homogenized and shows slightly increased compression due to the counterforce of the bracing. Since the curved parts of the jellyroll have no contact with the cell casing, no counterforce is exerted on this area by the bracing. This explains the similar results compared with the unconstrained cell. For theoretical consideration, the integration of a silicon foam layer with a thickness of 362 µm (lateral size equal to the flat jellyroll contact area) is integrated into the cell (Fig. 6c) instead of the outermost anode/separator/cathode layer and into the jellyroll void as well. No significant decrease of layer compression is observable.

From the mechanical point of view, the hardcase-type cell differs significantly from the pouch-type cell for several reasons. The hardcase-type cell has a comparably rigid casing that exerts significant counterforce when the electrodes expand during charging. Additionally, the counterforce is inhomogeneous owing to the prismatic shape of the casing. Hence, the counterforce of the casing is higher near the edges of the casing. Since the compression results of all three scenarios is similar, the main cause for inhomogeneous layer compression can be attributed to the flat-wound nature of the jellyroll. The flat-wound structure of the jelly roll leads to mixed effects because of irregular layer bending radii (like in a cylindrical cell) and a homogeneous layer structure (like in a pouch-type cell). Nevertheless, the void in the center of the jellyroll has a positive effect on the layer compression in the flat section of the jellyroll and acts as a kind of dilation buffer, even in the constrained cell. On the contrary, the addition of a foam layer is useless in this scenario because of this built-in buffer. But taking the irreversible dilation due to cell aging into account, the void in the middle of the jellyroll will be consumed over time. As a result, the usage of a single foam layer should mitigate and homogenize the pressure increase in aging hardcase-type cells as well for the flat jellyroll area.

3.3. Comparison of simulation results and localized lithium plating from post-mortem cells

Direct validation of the simulation results with real cells is hardly realizable owing to the large number of input parameters and the transient visco-elastic behavior of the materials. Additionally, it would need a cell-integrated spatial sensor layer, but without disturbing the cell electrochemistry which is hardly feasible for large format cells. To check if the results are plausible, one possibility is to compare the simulation results with localized plating in post-mortem cells. As discussed before, areas with a high gradient in layer compression are prone to the emergence of cell-internal balancing currents that can lead to localized lithium plating on the side of the lower material compression (i.e. higher ionic conductivity).

For the cylindrical cell, the area of the highest compression gradient is near the cell casing and casing edges. When compared with an opened 18650-cell after low temperature charging (Fig. 7a), an increased amount of plating can be found in this area.

Preprints (www.preprints.org) | NOT PEER-REVIEWED | Posted: 12 May 2021 doi:10.20944/preprints202011.0232.v2

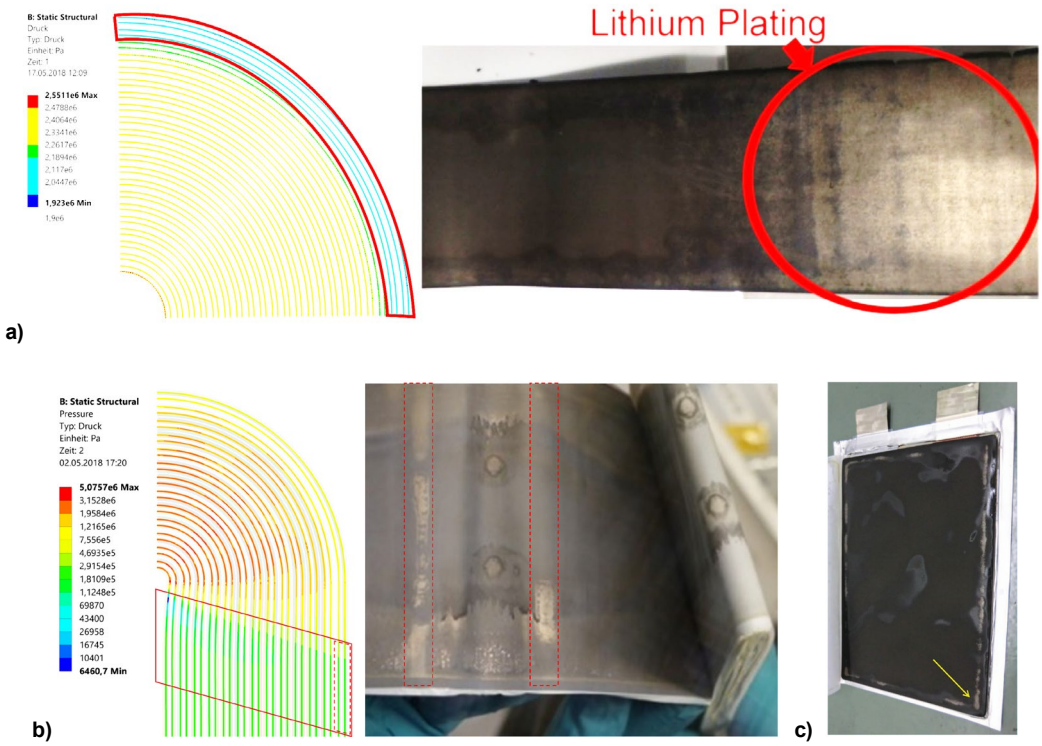

Fig. 7 (2 column): a) Area of high strain gradient and increased localized plating in the outer windings of an 18650 cell [18]. b) Localized lithium-plating areas in a post-mortem hardcase-type cell [33]. c) Localized lithium-plating areas in an opened pouch-type cell [32] (high strain = red, low strain = blue).

For a hardcase-type cell with a flat wound jellyroll, vertical stripes of localized lithium plating are found next to the curved jellyroll areas (Fig. 7b). Sticking to the hypothesis of high compression gradients as one root cause for lithium plating, the area with a high-pressure gradient in the simulation matches the empirically observed plating areas well. In all cell types, and especially in pouch-type cells (Fig. 7c), the effect of the pressure gradient in the anode overlap area can also be clearly observed by lithium-plating traces. Furthermore, comparing the results of a cell casing dilation measurement in a 94 Ah BEV hardcase-type cell with flat-wound jellyrolls with the results of mechanical simulation, the characteristic m-shape due to the flat-wound jellyroll (supplementary material Figure S.3) can be clearly observed. Despite the necessary simplifications used in the simulation process, the coinciding results proof the usability of the presented simulation method for qualitative investigations of (new) cell concepts.

3.4. Stacked hardcase-type HEV cell with foam layer and improved strain distribution

The previous results show clear advantages for the pouch-type cell from the mechanical and therefore electrochemical point of view. One disadvantage of the pouch-type cells is their delicate cell housing that is vulnerable to tearing or intrusive forces. This disadvantage is not present in the hardcase-type cells thanks to their intrinsically robust metal housing. But as shown before, the flat-wound electrode stack leads to inhomogeneous material strain during operation. To get the best out of both worlds, a simulation of a stacked hardcase-type HEV cell with and without a foam layer is conducted in an unbraced and braced scenario. The lateral dimensions of the electrodes are equal to the lateral dimensions of the flat-wound jellyroll.

For the unbraced hardcase-type cell with the stacked electrode layers, low and homogeneous material compression can be observed (Fig. 8a) in the center area. Moving towards the edges of the layers and hence towards the stiff casing edges, material compression increases before it reaches its maximum

Preprints (www.preprints.org) | NOT PEER-REVIEWED | Posted: 12 May 2021 doi:10.20944/preprints202011.0232.v2

at the anode overlap. The nonlinear increase in material compression of the separator in the outer layers results mainly from the nonlinear elastic behavior of the separator material.

When braced, a result (Fig. 8b) comparable with the braced pouch-type cell can be observed. Again, the compression of the separator is in the range of 9 % and 3 % for the electrodes. For the braced and unbraced cell, the sharp drop in compression due to the anode overlap can be clearly observed. Plating in this area should be visible as with commercial pouch-type cells.

Again, the beneficial effect of a foam layer (thickness 470 µm, area equal to cathode size) to allow for electrode expansion is clearly visible (Fig. 8c). Despite the stiff cell hardcase-type casing and bracing, favorable homogeneous and low layer compression can be achieved.

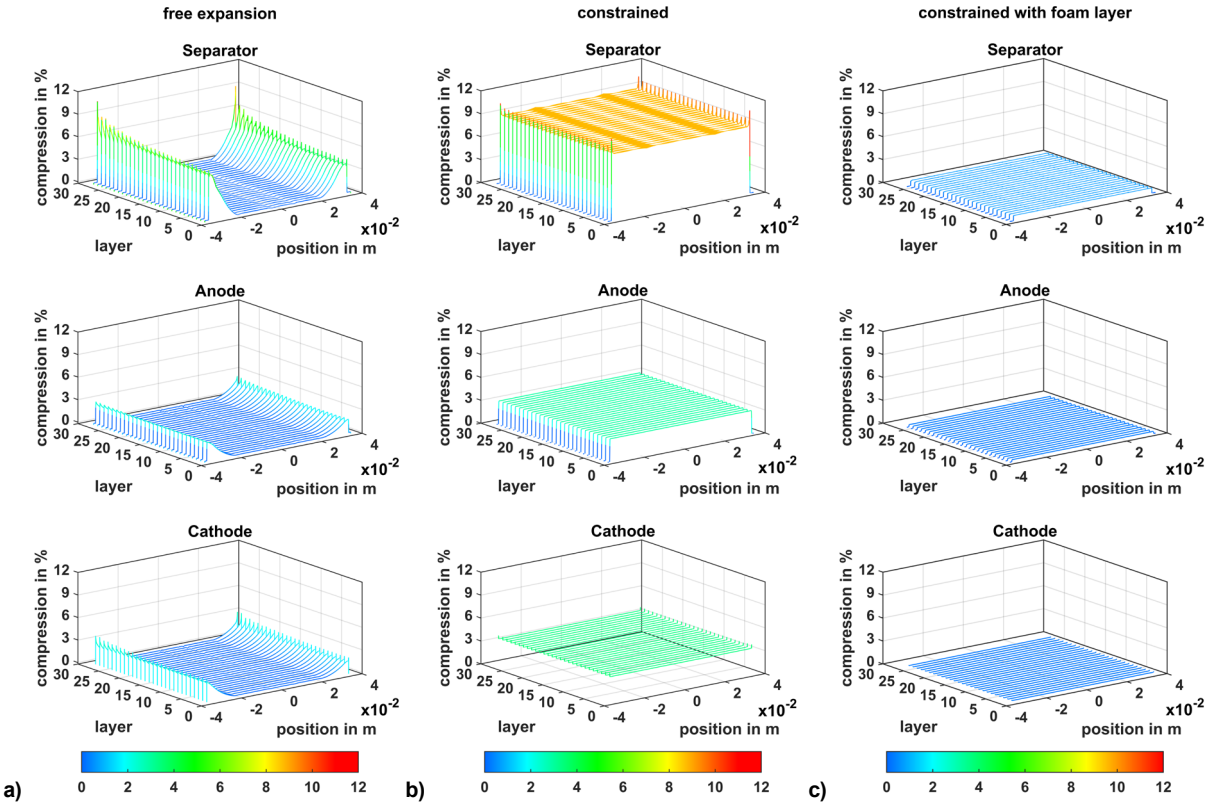

Fig. 8 (2 column) Final layer strain of a free stacked hardcase-type HEV cell a), b) constrained and c) a constrained stacked hardcase-type HEV cell with a foam layer to allow electrode expansion.

If maintaining cell size, the usage of a foam layer sheet instead of electrode layers leads to a loss of energy density. On the other hand, thinner separator layers could be used in this case since the material does not have to cope with electrode expansion even in braced cells. The usage of thinner separator layers would increase the cell's energy density and decrease the internal resistance of the cell. When calculated, the cell volume usage and therefore the energy density of the stacked HEV cell cross sectional model with the foam layer is even higher compared with the standard flat-wound HEV cell (Tab. 3) owing to better usage of the free volume in the cell casing corners.

Tab. 3 Calculated cell volume usage of electrode stack (equal to cell capacity) comparison of different hardcase-type HEV cell concepts for the cross-sectional model.

Flat-wound (original)	Flat-wound with foam layer	Stacked electrodes	Stacked electrodes with foam layer
64.6 %	59.1 %	70.5 %	65.4 %

 doi:10.20944/preprints202011.0232.v2

4. Conclusion

In this work, a layer resolved finite-element mechanical simulation to investigate spatial strain inhomogeneities in lithium-ion-cells due to electrode dilation dependent on internal and external cell structure was conducted. Depending on the electrode dilation characteristics during charging, the cell casing type, as well as the separator stiffness, distinctive strain patterns and gradients could be observed in the simulation results, which cannot be investigated by simplified homogenized mechanical simulation models. Furthermore, external mechanical forces were found to have a significant impact on the cell-internal layer strain amount and distribution.

Areas of high strain gradients in the simulation were found to coincide with localized lithium-plating areas observed in post-mortem cells. Since locally strained separator areas lead to localized balancing currents, a low and homogeneous cell layer strain found e.g. in pouch-type cells should be favorable for cell aging compared with other cell types. When cells must be braced, e.g. in automotive applications, additional measures like foam layers could be applied to mitigate and homogenize elevated layer stress due to the bracing counterforces. A hypothetical stacked hardcase-type HEV cell with a foam layer instead of some electrode layers that combines the intrinsic rigidity of a hardcase-type cell with the homogeneous layer strain of a pouch-type cell is shown to achieve an even higher cell volume usage compared with the classic flat-wound HEV hardcase-type cell despite the added foam layer.

With the used purely mechanical model, a cell format dependent identification of mechanical and therefore electrochemical weak points with reasonable simulation effort is possible for new cell concepts. The simulation results are sensitive to material parameters and should be treated as qualitative results. Therefore, if quantitative results are required, measurement and parameterization of the specific cell material parameters is essential. In future work, the model could be extended with an electrochemical coupled sub-model to simulate transient effects like cell aging. Additionally, effects due to thermal inhomogeneities caused by mechanically induced local current density inhomogeneities could be implemented in future models. The locally increased temperature has impact on the spatial mechanical stiffness of the battery materials (especially the polymeric based separator) and therefore could cause additional layer strain.

CRediT author statement

Fabian Ebert: Conceptualization, Methodology, Investigation, Writing - Original Draft, Writing - Review & Editing, Visualization, Supervision, Funding acquisition **Markus Spielbauer**: Methodology, Investigation, Writing - Original Draft, Writing - Review & Editing, Visualization **Maximilian Bruckmoser:** Methodology, Investigation, Writing - Original Draft, Visualization **Markus Lienkamp**: Conceptualization, Resources, Supervision, Writing - Review & Editing

Acknowledgements

This work was supported by the Federal Ministry for Economic Affairs and Energy of Germany in the project REVISEDBATT [grant number 03ETE004A].

References

[1] Y.N. Jo, Y. Kim, J.S. Kim, J.H. Song, K.J. Kim, C.Y. Kwag, D.J. Lee, C.W. Park, Y.J. Kim, Si-graphite composites as anode materials for lithium secondary batteries, J. Power Sources. 195 (2010) 6031–6036. https://doi.org/10.1016/j.jpowsour.2010.03.008.

[2] D. Sauerteig, S. Ivanov, H. Reinshagen, A. Bund, Reversible and irreversible dilation of lithium-ion battery electrodes investigated by in-situ dilatometry, J. Power Sources. 342 (2017) 939–946. https://doi.org/10.1016/j.jpowsour.2016.12.121.

[3] B. Rieger, S. Schlueter, S.V. Erhard, J. Schmalz, G. Reinhart, A. Jossen, Multi-scale investigation of thickness changes in a commercial pouch type lithium-ion battery, J. Energy Storage. 6 (2016) 213–221. https://doi.org/10.1016/j.est.2016.01.006.

[4] M. Hahn, H. Buqa, P.W. Ruch, D. Goers, M.E. Spahr, J. Ufheil, P. Novák, R. Kötz, A Dilatometric Study of Lithium Intercalation into Powder-Type Graphite Electrodes, Electrochem. Solid-State Lett. 11 (2008) A151. https://doi.org/10.1149/1.2940573.

[5] H.-D. Yoo, J.-H. Ryu, S.-H. Park, Y.-W. Park, B.-H. Ka, S.-M. Oh, Expanded Graphite Negative Electrode for Lithium-ion Batteries, J. Electrochem. Sci. Technol. 2 (2011) 45–50. https://doi.org/10.5229/JECST.2011.2.1.045.

[6] S. Schweidler, L. de Biasi, A. Schiele, P. Hartmann, T. Brezesinski, J. Janek, Volume Changes of Graphite Anodes Revisited: A Combined Operande X-ray Diffraction and In-situ Pressure Analysis Study, J. Phys. Chem. (2018). https://doi.org/10.1021/acs.jpcc.8b01873.

[7] R. Yazami, Y. Reynier, Thermodynamics and crystal structure anomalies in lithium-intercalated graphite, J. Power Sources. 153 (2006) 312–318. https://doi.org/10.1016/j.jpowsour.2005.05.087.

[8] M. Ashuri, Q. He, L.L. Shaw, Silicon as a potential anode material for Li-ion batteries: where size, geometry and structure matter, Nanoscale. 8 (2016) 74–103. https://doi.org/10.1039/C5NR05116A.

[9] D. Uxa, B. Jerliu, E. Hüger, L. Dörrer, M. Horisberger, J. Stahn, H. Schmidt, On the Lithiation Mechanism of Amorphous Silicon Electrodes in Li-Ion Batteries, J. Phys. Chem. C. 123 (2019) 22027–22039. https://doi.org/10.1021/acs.jpcc.9b06011.

[10] M. Nagayama, K. Ariyoshi, Y. Yamamoto, T. Ohzuku, Characterization of Lithium Insertion Electrodes by Precision Dilatometer: Area-Specific Deformation of Single Electrode, J. Electrochem. Soc. 161 (2014) A1388–A1393. https://doi.org/10.1149/2.0981409jes.

[11] J.-M. Kim, H.-T. Chung, Role of transition metals in layered Li[Ni,Co,Mn]O2 under electrochemical operation, Electrochim. Acta. 49 (2004) 3573–3580. https://doi.org/10.1016/j.electacta.2004.03.025.

[12] J.N. Reimers, Electrochemical and In Situ X-Ray Diffraction Studies of Lithium Intercalation in LixCoO2, J. Electrochem. Soc. 139 (1992) 2091–2097. https://doi.org/10.1149/1.2221184.

[13] M.N. Obrovac, L. Christensen, Structural Changes in Silicon Anodes during Lithium Insertion/Extraction, Electrochem. Solid-State Lett. 7 (2004) A93–A96. https://doi.org/10.1149/1.1652421.

[14] J. Vetter, P. Novák, M.R. Wagner, C. Veit, K.-C. Möller, J.O. Besenhard, M. Winter, M. Wohlfahrt-Mehrens, C. Vogler, A. Hammouche, Ageing mechanisms in lithium-ion batteries, J. Power Sources. 147 (2005) 269–281. https://doi.org/10.1016/j.jpowsour.2005.01.006.

[15] F. Ebert, A. Oberbauer, M.A. Cabañero, G. Sextl, M. Lienkamp, Simulation of Lithium Plating Due to Spatial Inhomogeneous Separator Strain in Lithium-Ion-Cells, Int. J. Automot. Eng. 10 (2019) 242–248. https://doi.org/10.20485/jsaeijae.10.2_242.

[16] J. Cannarella, X. Liu, C.Z. Leng, P.D. Sinko, G.Y. Gor, C.B. Arnold, Mechanical Properties of a Battery Separator under Compression and Tension, J. Electrochem. Soc. 161 (2014) F3117–F3122. https://doi.org/10.1149/2.0191411jes.

[17] J. Cannarella, C.B. Arnold, The Effects of Defects on Localized Plating in Lithium-Ion Batteries, J. Electrochem. Soc. 162 (2015) A1365–A1373. https://doi.org/10.1149/2.1051507jes.

[18] T.C. Bach, S.F. Schuster, E. Fleder, J. Müller, M.J. Brand, H. Lorrmann, A. Jossen, G. Sextl, Nonlinear aging of cylindrical lithium-ion cells linked to heterogeneous compression, J. Energy Storage. 5 (2016) 212–223. https://doi.org/10.1016/j.est.2016.01.003.

[19] F. Ebert, G. Sextl, M. Lienkamp, Effect of a flexible battery module bracing on cell aging, in: 2017 Twelfth Int. Conf. Ecol. Veh. Renew. Energies, IEEE, 2017: pp. 1–5. https://doi.org/10.1109/EVER.2017.7935871.

[20] J. Cannarella, C.B. Arnold, Stress evolution and capacity fade in constrained lithium-ion pouch cells, J. Power Sources. 245 (2014) 745–751. https://doi.org/10.1016/j.jpowsour.2013.06.165.

[21] G. Fuchs, L. Willenberg, F. Ringbeck, D.U. Sauer, Post-Mortem Analysis of Inhomogeneous Induced Pressure on Commercial Lithium-Ion Pouch Cells and Their Effects, Sustainability. 11 (2019) 6738. https://doi.org/10.3390/su11236738.

[22] M. Loveridge, G. Remy, N. Kourra, R. Genieser, A. Barai, M. Lain, Y. Guo, M. Amor-Segan, M. Williams, T. Amietszajew, M. Ellis, R. Bhagat, D. Greenwood, Looking Deeper into the Galaxy (Note 7), Batteries. 4 (2018) 1–11. https://doi.org/10.3390/batteries4010003.

[23] X. Zhang, E. Sahraei, K. Wang, Li-ion Battery Separators, Mechanical Integrity and Failure Mechanisms Leading to Soft and Hard Internal Shorts, Sci. Rep. 6 (2016) 32578. https://doi.org/10.1038/srep32578.

[24] M.J. Brand, S.F. Schuster, T. Bach, E. Fleder, M. Stelz, S. Gläser, J. Müller, G. Sextl, A. Jossen, Effects of vibrations and shocks on lithium-ion cells, J. Power Sources. 288 (2015) 62–69.

https://doi.org/10.1016/j.jpowsour.2015.04.107.

[25] J. Hooper, J. Marco, G. Chouchelamane, C. Lyness, Vibration Durability Testing of Nickel Manganese Cobalt Oxide (NMC) Lithium-Ion 18,650 Battery Cells, Energies. 9 (2016) 52. https://doi.org/10.3390/en9010052.

[26] F. Ebert, G. Sextl, M. Lienkamp, Influence Of Dynamic Mechanical Stress On Lithium-Ion-Battery Aging: CoFAT 2017, in: Conf. Futur. Automot. Technol., Fürstenfeldbruck, 2017: pp. 1–6.

[27] H. Wang, A. Kumar, S. Simunovic, S. Allu, S. Kalnaus, J.A. Turner, J.C. Helmers, E.T. Rules, C.S. Winchester, P. Gorney, Progressive mechanical indentation of large-format Li-ion cells, J. Power Sources. 341 (2017) 156–164. https://doi.org/10.1016/j.jpowsour.2016.11.094.

[28] L. Greve, C. Fehrenbach, Mechanical testing and macro-mechanical finite element simulation of the deformation, fracture, and short circuit initiation of cylindrical Lithium ion battery cells, J. Power Sources. 214 (2012) 377–385. https://doi.org/10.1016/j.jpowsour.2012.04.055.

[29] A. Barai, R. Tangirala, K. Uddin, J. Chevalier, Y. Guo, A. McGordon, P. Jennings, The effect of external compressive loads on the cycle lifetime of lithium-ion pouch cells, J. Energy Storage. 13 (2017) 211–219. https://doi.org/10.1016/j.est.2017.07.021.

[30] A.S. Mussa, M. Klett, G. Lindbergh, R.W. Lindström, Effects of external pressure on the performance and ageing of single-layer lithium-ion pouch cells, J. Power Sources. 385 (2018) 18–26. https://doi.org/10.1016/j.jpowsour.2018.03.020.

[31] G. Kermani, E. Sahraei, Review: Characterization and modeling of the mechanical properties of lithium-ion batteries, Energies. 10 (2017). https://doi.org/10.3390/en10111730.

[32] C. Birkenmaier, B. Bitzer, M. Harzheim, A. Hintennach, T. Schleid, Lithium Plating on Graphite Negative Electrodes: Innovative Qualitative and Quantitative Investigation Methods, J. Electrochem. Soc. 162 (2015) A2646–A2650. https://doi.org/10.1149/2.0451514jes.

[33] E. Knobbe, private communication, (2017).

[34] D. Sauerteig, N. Hanselmann, A. Arzberger, H. Reinshagen, S. Ivanov, A. Bund, Electrochemical-mechanical coupled modeling and parameterization of swelling and ionic transport in lithium-ion batteries, J. Power Sources. 378 (2018) 235–247. https://doi.org/10.1016/j.jpowsour.2017.12.044.

[35] Y. Qi, L.G. Hector, C. James, K.J. Kim, Lithium Concentration Dependent Elastic Properties of Battery Electrode Materials from First Principles Calculations, J. Electrochem. Soc. 161 (2014) F3010–F3018. https://doi.org/10.1149/2.0031411jes.

[36] K.Y. Oh, B.I. Epureanu, Characterization and modeling of the thermal mechanics of lithium-ion battery cells, Appl. Energy. 178 (2016) 633–646. https://doi.org/10.1016/j.apenergy.2016.06.069.

[37] A. Santimetaneedol, R. Tripuraneni, S.A. Chester, S.P.V. V Nadimpalli, Time-dependent deformation behavior of polyvinylidene fluoride binder: Implications on the mechanics of composite electrodes, J. Power Sources. 332 (2016) 118–128. https://doi.org/10.1016/j.jpowsour.2016.09.102.

[38] P. Berg, J. Soellner, A. Jossen, Structural dynamics of lithium-ion cells – Part I : Method , test bench validation and investigation of lithium-ion pouch cells, J. Energy Storage. 26 (2019) 100916. https://doi.org/10.1016/j.est.2019.100916.

[39] T. Deich, S.L. Hahn, S. Both, K.P. Birke, A. Bund, Validation of an actively-controlled pneumatic press to simulate automotive module stiffness for mechanically representative lithium-ion cell aging, J. Energy Storage. 28 (2020) 101192. https://doi.org/10.1016/j.est.2020.101192.

[40] D.P. Finegan, E. Tudisco, M. Scheel, J.B. Robinson, O.O. Taiwo, D.S. Eastwood, P.D. Lee, M. Di Michiel, B. Bay, S.A. Hall, G. Hinds, D.J.L. Brett, P.R. Shearing, M. Di Michiel, B. Bay, S.A. Hall, G. Hinds, Brett, Dan J. L., P.R. Shearing, Quantifying bulk electrode strain and material displacement within lithium batteries via high-speed operando tomography and digital volume correlation, Adv. Sci. 3 (2015) 1–11. https://doi.org/10.1002/advs.201500332.

[41] M. Tang, P. Albertus, J. Newman, Two-Dimensional Modeling of Lithium Deposition during Cell Charging, J. Electrochem. Soc. 156 (2009) A390. https://doi.org/10.1149/1.3095513.

[42] J. Cannarella, C.B. Arnold, Ion transport restriction in mechanically strained separator membranes, J. Power Sources. 226 (2013) 149–155. https://doi.org/10.1016/j.jpowsour.2012.10.093.

Preprints (www.preprints.org) | NOT PEER-REVIEWED | Posted: 12 May 2021 doi:10.20944/preprints202011.0232.v2

Supplementary material

1. Layer thickness parameters

Table S.1 (2 column): Layer thickness definitions for different electrode configurations.

	Anode loading (per side)	Current collector anode E = 113 GPa	Cathode loading (per side)	Current collector cathode E = 70 GPa	Separator
high Energy (hE)					
thickness in µm	80	20	60	22	20
high Power (hP)					
thickness in µm	45	25	25	30	20

Cylindrical cross-sectional cell model parameters

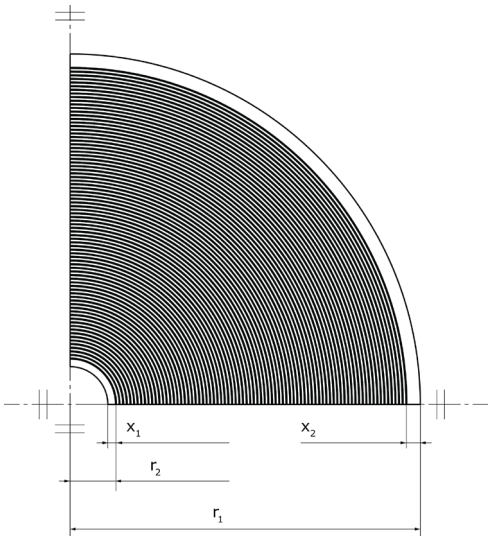

Table S.2 (2 column): Dimensional parameters cylindrical cross-sectional cell model.

Parameter	Value in mm	Parameter	Value in mm
x_1	0.2	r_1	9.045
x_2	0.35	r_2	1.175

Preprints (www.preprints.org) | NOT PEER-REVIEWED | Posted: 12 May 2021 doi:10.20944/preprints202011.0232.v2

2. Cylindrical longitudinal cross-sectional cell model parameters

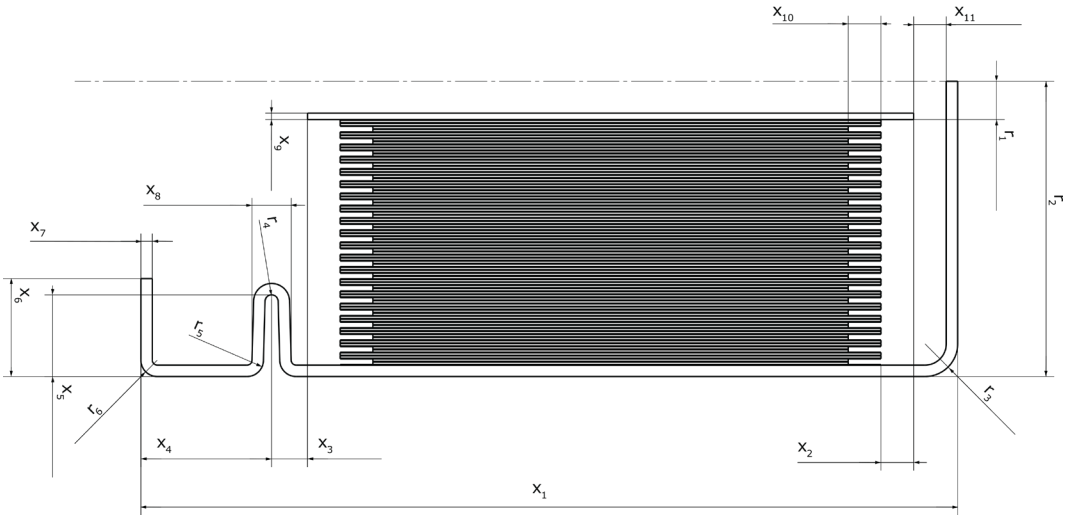

Table S.3 (2 column): Dimensional parameters cylindrical longitudinal cross-sectional cell model.

Parameter	Value in mm	Parameter	Value in mm
x_1	65	r_1	1.175
x_2	1	r_2	9.045
x_3	1	r_3	1
x_4	5	r_4	0.5
x_5	2.5	r_5	0.5
x_6	3	r_6	1.5
x_7	0.35		
x_8	1.5		
x_9	0.2		
x_{10}	1		
x_{11}	2		

Preprints (www.preprints.org) | NOT PEER-REVIEWED | Posted: 12 May 2021 doi:10.20944/preprints202011.0232.v2

3. Pouch-type cell model parameters

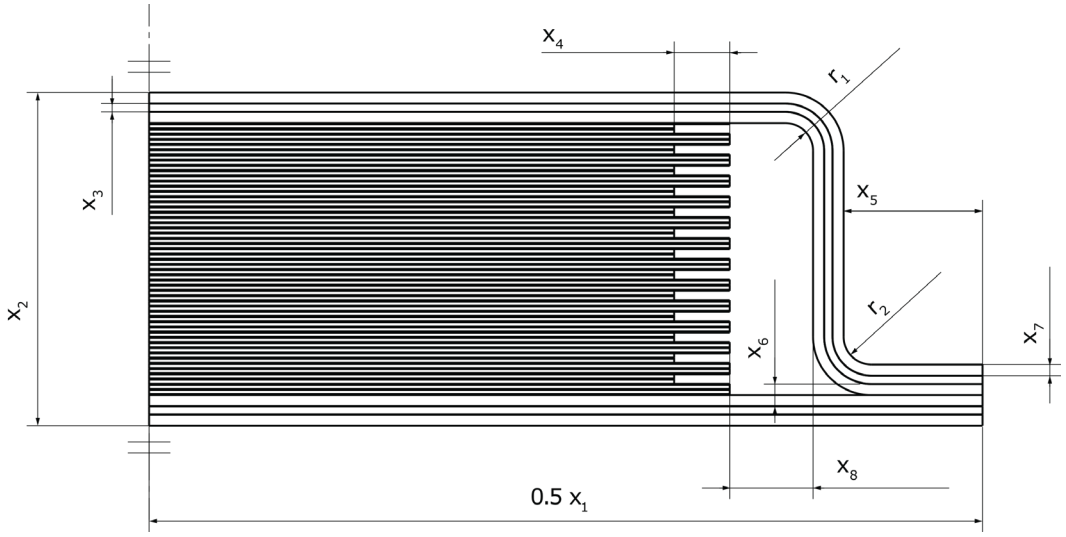

Table S.4 (2 column): Dimensional parameters pouch-type cell model.

Parameter	Value in mm	Parameter	Value in mm
x_1	84	r_1	0.5
x_2	65	r_2	0.5
x_3	0.075		
x_4	1		
x_5	3		
x_6	0.075		
x_7	0.075		
x_8	2		

Preprints (www.preprints.org) | NOT PEER-REVIEWED | Posted: 12 May 2021 doi:10.20944/preprints202011.0232.v2

4. Hardcase-type HEV cell model parameters

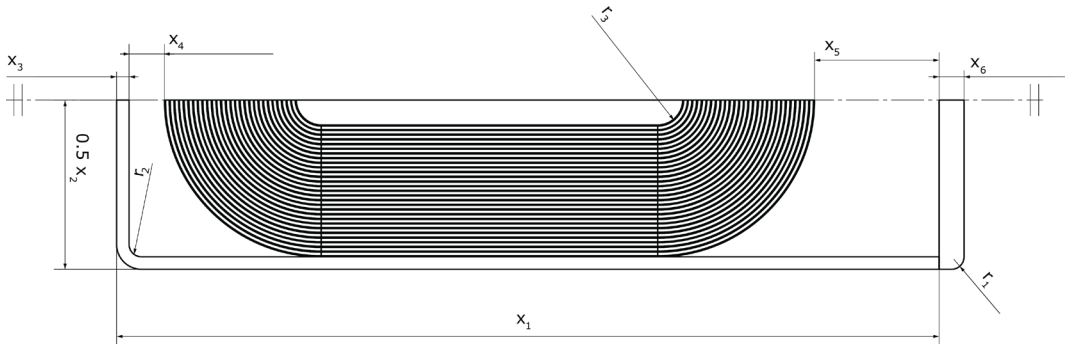

Table S.5 (2 column): Dimensional parameters hardcase-type HEV cell model.

Parameter	Value in mm	Parameter	Value in mm
x_1	80.5	r_1	0.5
x_2	12	r_2	1
x_3	1	r_3	0.25
x_4	1		
x_5	5.5		
x_6	2		

5. Hardcase-type HEV stacked cell model parameters

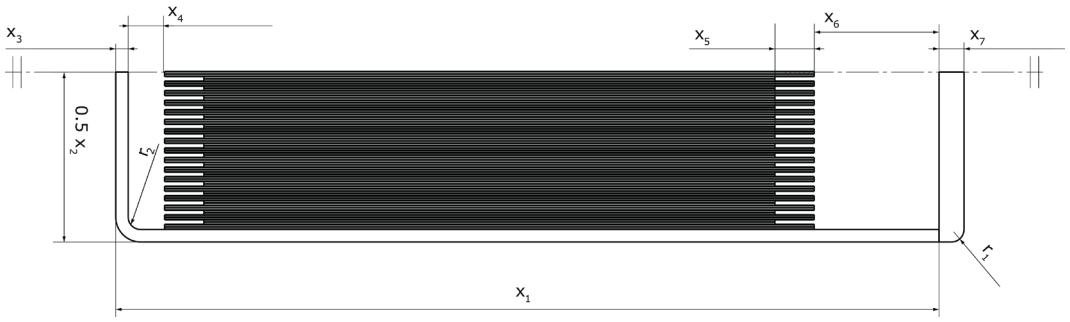

Table S.6 (2 column): Dimensional parameters hardcase-type stacked HEV cell model.

Parameter	Value in mm	Parameter	Value in mm
x_1	80.5	r_1	0.5
x_2	12	r_2	1
x_3	1		
x_4	1.5		
x_5	1		
x_6	5.5		
x_7	2		

Preprints (www.preprints.org) | NOT PEER-REVIEWED | Posted: 12 May 2021 doi:10.20944/preprints202011.0232.v2

6. Ogden-foam parameters for polymer materials

Table S.7 (2 column): Ogden-foam parameters for separator and silicon foam materials.

Parameter	PE-Separator	PP-Separator	HT800-Silicon foam
μ_1 in Pa	- 500000	17500000	46000
α_1	15	29	17
μ_2 in Pa	- 42500000	2800000	- 10500
α_2	- 1.4	- 3.7	- 2.9
μ_3 in Pa	9800000	- 875000	3650
α_3	- 2.9	- 6.2	- 2.8

7. Simulation hypotheses and boundary definitions

Table S.8 (2 column): Boundary definitions for the different cell models

Contact pair	Contact type	Contact formulation	Contact detection method
Electrode material – Collector	bonded	Internal Multipoint Constraint (MPC)	Node-to-Surface
Separator - Electrode material	frictional	Normal-Lagrange	Node-to-Surface
Anode collector – Casing	frictional	Normal-Lagrange	Node-to-Surface
Foam – Casing	frictional	Normal-Lagrange	Node-to-Surface
Foam – Anode collector	bonded	Internal Multipoint Constraint (MPC)	Node-to-Surface

Table S.9 (2 column): Simulation hypotheses for the different cell models

Model	Simulation hypothesis
Cylindrical cell – cross-sectional model	Plane strain
Cylindrical cell – longitudinal model	axisymmetric
Pouch-type cell – longitudinal model	Plane strain
Hardcase-type cell (flat-wound) – longitudinal model	Plane strain
Hardcase-type cell (stacked) – longitudinal model	Plane strain

8. Supplementary figures

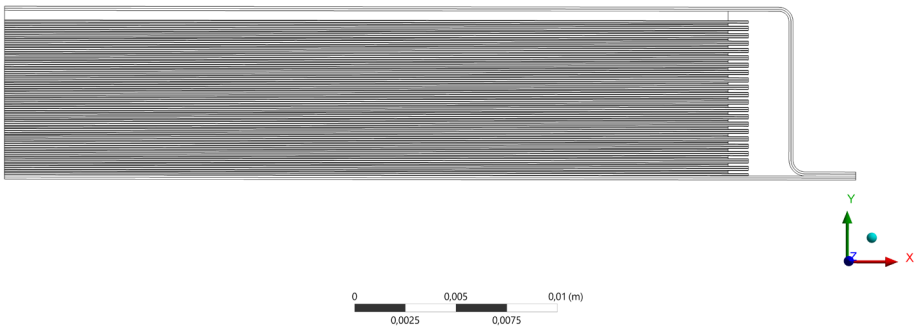

Figure S.1 (2 column): Pouch-type cell with anode-sized foam layer between electrodes and cell casing (top side).

Preprints (www.preprints.org) | NOT PEER-REVIEWED | Posted: 12 May 2021 doi:10.20944/preprints202011.0232.v2

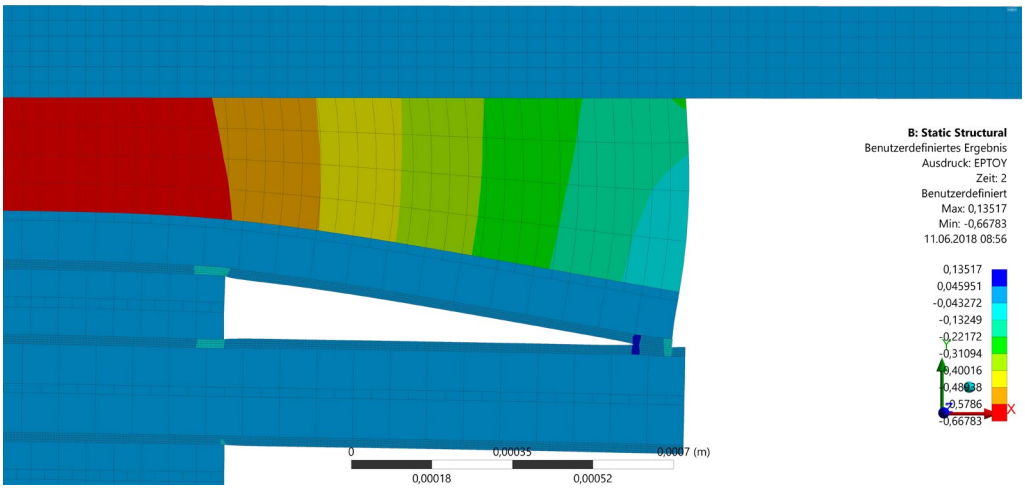

Figure S.2 (2 column): Pressure increase in cathode edges owing to cathode sized foam layer.

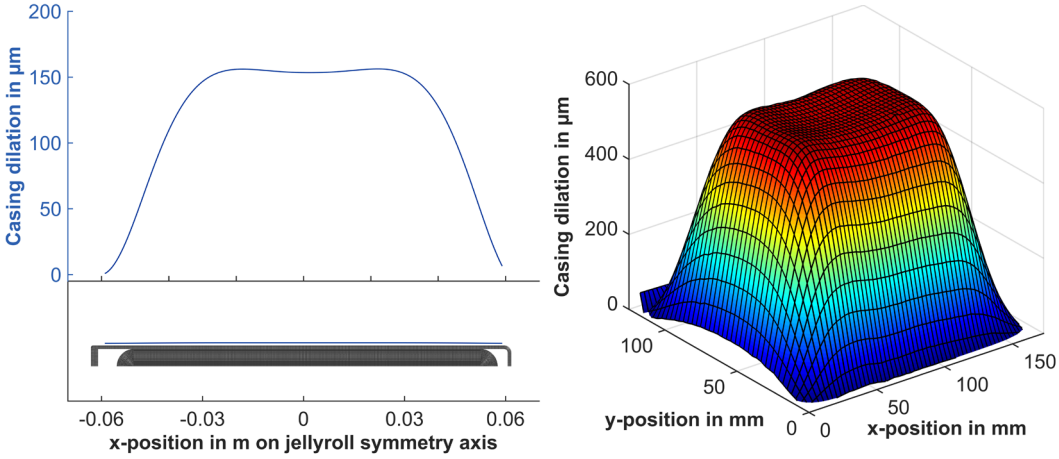

Figure S.3 (2 column): Simulated (HEV-cell) and measured (94 Ah BEV-cell) casing expansion with characteristic m-shape after cell charging. A working HEV-cell was not available for measurements.

Preprints (www.preprints.org) | NOT PEER-REVIEWED | Posted: 12 May 2021 doi:10.20944/preprints202011.0232.v2

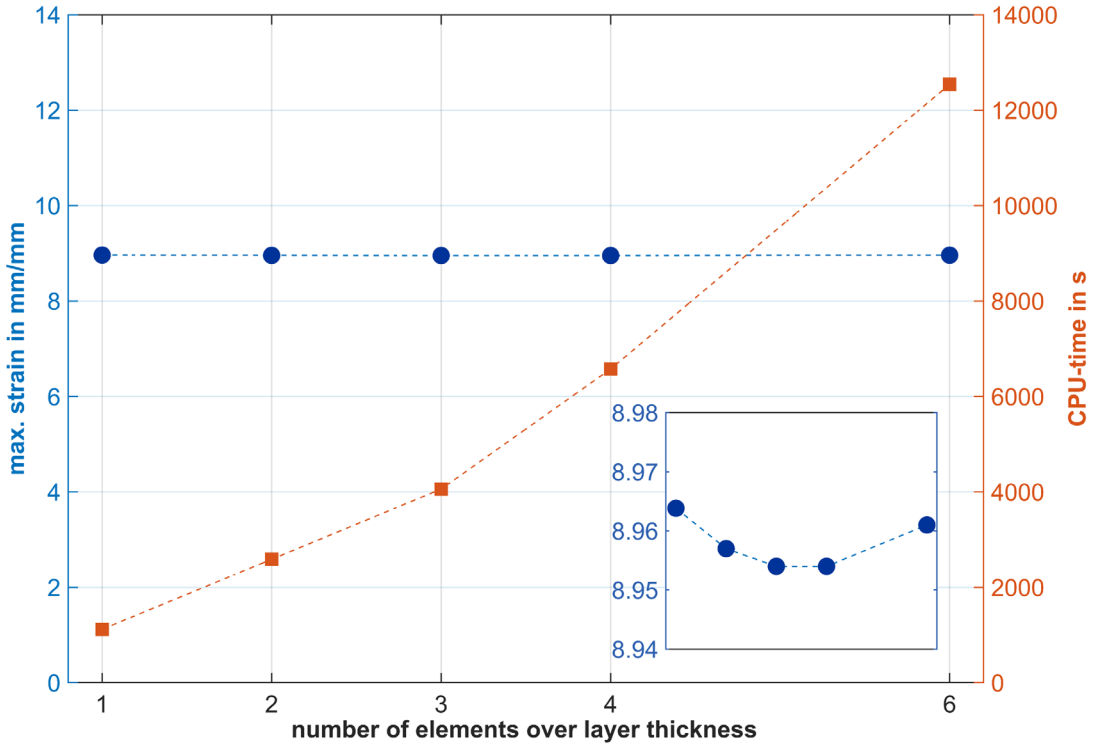

Figure S.4 (2 column): Convergence study to determine optimal mesh size for the cross-sectional model.

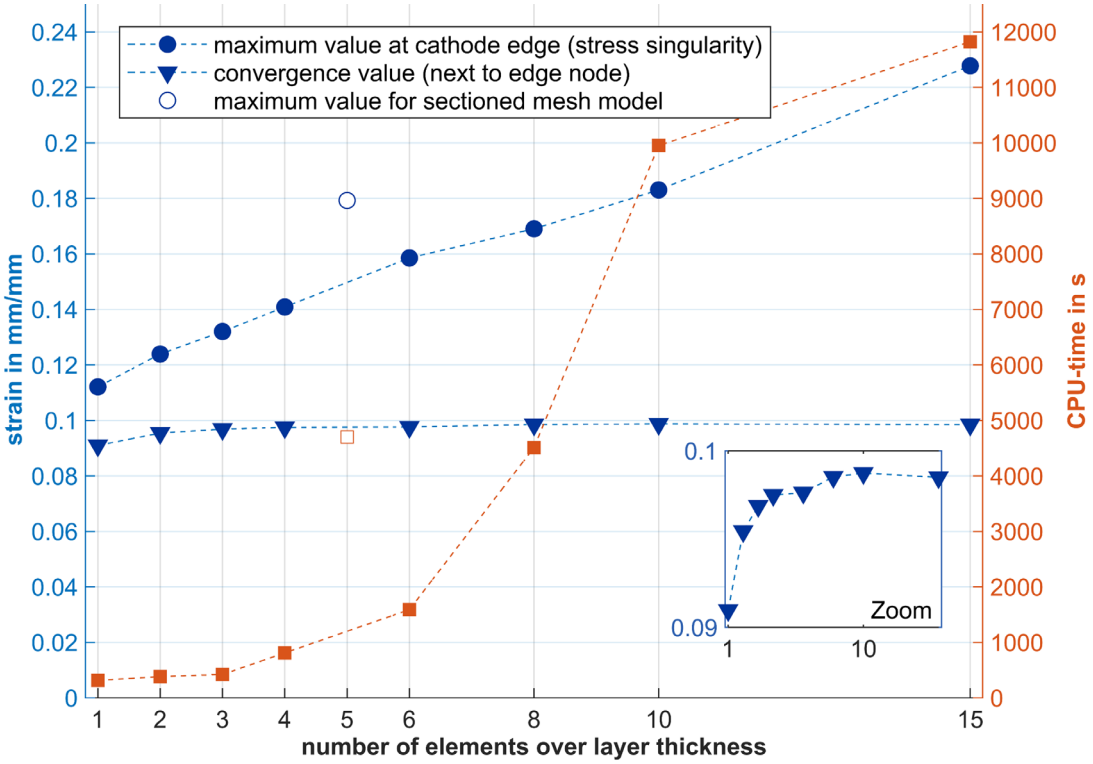

Figure S.5 (2 column): Convergence study to determine optimal mesh size for the longitudinal sectional model. The converging value of the node next to the cathode edge node (nonconverging maximum value due to stress singularity) is used as strain result instead.